Power Electronic Systems
Laboratory

IEEE Transactions on Magnetics, Vol. 49, No. 10, pp. 5248-5256, October 2013

Full PEEC Modeling of EMI Filter Inductors in the Frequency Domain

I. Kovacevic,
T. Friedli,
A. Müsing,
J. W. Kolar

Eidgenössische Technische Hochschule Zürich
Swiss Federal Institute of Technology Zurich

Full PEEC Modeling of EMI Filter Inductors in the Frequency Domain

Ivana F. Kovačević[1], Thomas Friedli[2], Andreas M. Müsing[1], and Johann W. Kolar[1], *Fellow, IEEE*

[1]ETH Zurich, Power Electronic Systems Laboratory, 8092 Zurich, Switzerland
[2]ABB Switzerland Ltd., Leistungselektronik & MS-Antriebe, Turgi, Aargau 5300, Switzerland

In this paper, the performance of a new method based on the coupling of the partial element equivalent circuit method and boundary integral method (the PEEC-BIM method) for 3D modeling of toroidal inductors, which are typically used in electromagnetic interference (EMI) filter applications, is presented. The presence of magnetic materials is modeled by replacing the surface of magnetic regions with an equivalent distribution of fictitious current loops. It is shown that the influence of the magnetic core on the impedance and the stray field of EMI filter inductors can be modeled and explained in detail by PEEC-BIM simulation results. The developed PEEC-BIM approach is verified by both 3D finite-element method (FEM) simulations and near-field measurements for different winding configurations and magnetic cores. Regarding computational complexity, the developed PEEC-BIM method applied to toroidal inductors performs extremely well. The PEEC-BIM simulation is at least twice faster than the corresponding FEM-based analysis. The PEEC-BIM method has been implemented in a PEEC-based simulation tool, which facilitates the simulation of entire EMI filter structures.

***Index Terms*—Boundary integral method (BIM), effective permeability, magnetic coupling, partial element equivalent circuit (PEEC) method.**

I. Introduction

NOWADAYS, with an increasing tendency in power electronics towards high-power density and fast-switching power electronic devices, the design of power electronic systems according to electromagnetic compatibility (EMC) standards requires longer design time and great engineering experience. As EMC problems cannot be solved in an easy and straightforward way, there is a need to consider different engineering fields simultaneously, i.e., power electronics, and computational electromagnetics, in order to obtain good and optimal design solutions. Electromagnetic Interference (EMI) problems originate from inadequate PCB layout, components' parasitics, and mutual electromagnetic coupling effects. However, conducting high-frequency EM noise cannot be reduced only by means of a proper PCB layout and shielding techniques. Power electronic (PE) systems typically require an EMI input filter to meet the EMC standards. The prediction of the electromagnetic (EM) behavior prior to hardware prototyping is a critical design step in order to reduce the development time. It has been shown that both self-parasitic and mutual EM coupling effects have influence on the EMI filter attenuation characteristic and must be taken into account [1]. Accordingly, the idea behind the work presented in this paper is to build a modeling and simulation environment for virtual prototyping of EMI filters and power electronic converter systems. The first step towards this EM simulation tool is to develop 3D models of power electronic components, which can accurately represent both their electrical and EM properties. The partial element equivalent circuit (PEEC) method has proven to be an efficient numerical approach for solving circuit-field problems, e.g., for PCB layouts, EMI filters, etc. [2]. The PEEC method was originally developed for EM modeling of complex IC interconnections, and so far, several extensions have been proposed, e.g. for dielectrics [3] and nonorthogonal geometries [2], [4]. However, PEEC-based modeling of nonlinearity, anisotropy, and other magnetic properties is not an easy task and is not performed in practice. As a result, exact 3D PEEC-based models of magnetic components used in power electronics do not exist, and the finite-element method (FEM) is typically applied for this class of problems. Since the practical design of inductors and transformers is based on frequency dependent permeability curves $\mu_{\mathrm{r}}(f)$ given by manufacturers, or on $\mu_{\mathrm{r}}(f)$ measurements, the modeling of a magnetic core using $\mu_{\mathrm{r}}(f)$, i.e. as a linear and homogeneous material, is fully justified for PE applications. This simplifies the PEEC-based modeling of magnetic PE components in the frequency domain. Accordingly, in this paper, a new extension of the PEEC method is described, together with its implementation intended for 3D modeling of toroidal inductors employed for the design of EMI input filters.

II. State-of-the-Art

The PEEC method is derived from the integral formulation of Maxwell's equations. In comparison to the differential field solvers like FEM, the PEEC method does not need to mesh a vacuum volume region around the dielectric and/or magnetic material but just the conducting, dielectric and/or magnetic regions [5]. This reduces the computational complexity significantly. Furthermore, the PEEC method leads to an equivalent electric circuit problem that can be easily interfaced to any circuit solver such as SPICE or GeckoCIRCUITS [6]. However, the main difficulty for the PEEC modeling approach is the presence of magnetic materials, like the ferromagnetic cores, which are used in many EMI filter applications. For this class of problems, FEM is typically used, and the FEM-PEEC [7] coupled method was recently developed in order to take advantage of two modeling methodologies. By such an approach, the problem of a complex FEM mesh is not fully avoided but is lessened in the way that the mesh around conductors is relaxed. Regarding EMI noise prediction, common (CM) and differential

Manuscript received October 17, 2012; revised March 08, 2013; accepted April 16, 2013. Date of publication April 26, 2013; date of current version September 20, 2013. Corresponding author: I. F. Kovačević (e-mail: kovacevic@lem.ee.ethz.ch).

Color versions of one or more of the figures in this paper are available online at http://ieeexplore.ieee.org.

Digital Object Identifier 10.1109/TMAG.2013.2260344

(DM) mode currents have to be considered [8], and the major limitation is the modeling of the stray field of passive filter components generated by these currents.

A DM inductor used to attenuate DM current noise should be able to handle the rated current of the system that produces a significant 50-Hz flux-density, without magnetic saturation. Thus, the typical DM inductors are built on lower permeability toroidal cores with distributed air gap, and a uniform winding arrangement. A single-phase CM inductor is typically designed as a single magnetic core structure wound with two coupled windings in series to each power line. The low amplitude of CM currents allows the design of CM chokes using high permeability toroidal cores. A clear understanding of the stray field generated by toroidal inductors is still missing, and the corresponding PEEC models have been only developed approximately [9], [10].

In [9], the PEEC modeling of the stray field of CM toroidal inductors was performed under the assumption that the magnetic core does not change the direction of magnetic field lines and that the influence of the core can be described by a correction factor of the effective permeability $\mu_{\rm eff}$, which was considered to depend only on the geometry of the core and the coil. In [10], the authors ignored the presence of the core assuming that it has insignificant influence on the magnetic coupling in order to perform fast EMC optimization of a power converter. The motivation of the research presented in this paper is to evaluate these approximations and their applicability for both uniform and nonuniform winding arrangements, i.e. respectively, the DM and single-phase CM winding arrangements.

Accordingly, the coupled PEEC and boundary integral method (PEEC-BIM) method, first introduced in [11], is further simplified and verified by measurements of the inductor impedance and mutual coupling effects in this paper. In the following sections, it is shown that the proposed modeling approach can be used to fully model the EM behavior of toroidal inductors including both their internal, i.e., inductance, and external, i.e., stray/leakage, properties. The approach also enables an evaluation of the previously mentioned approximations.

III. PEEC-BIM Method for EMI Filter Inductors

The theory behind the PEEC-BIM model was introduced and verified in [11] by the impedance measurements of toroidal EMI filter inductors. The focus of the research presented in this paper is the verification of the proposed PEEC-BIM method by both the inductance and mutual coupling effect measurements. This leads to a full 3D EM model of inductors and, moreover, to 3D models of complete EMI filters. From EM theory, the influence of the core can be explained by the magnetization vector $\vec{M}$, which, in turn, can be modeled by a distribution of fictitious magnetic currents (and/or charges) existing within the volume and on the surface of the magnetic core. It was shown that the calculation of the magnetic volume densities does not have to be performed for linear homogeneous magnetic materials so that the problem can be reduced to the representation of the core by the surface current (charge) density $\vec{K}_{\rm M}$ $(\sigma_{\rm M})$ [12].

The extended PEEC method for modeling in the presence of magnetic materials based on the magnetic current approach is used to derive the so-called "MagPEEC" method in [13] for RF inductors, and it is explained in [14] on some simple geometry examples. Even though the theoretical background of the magnetic current approach is well known from electromagnetic theory, the difficulties arise with the numerical implementation of the extended PEEC method for the standard PE magnetic component geometries, i.e., the mesh of the magnetic volume, the selection of basis-functions for the numerical implementation, and the singularity problem for the calculation of matrix elements. The simplified PEEC-BIM coupled method and its implementation into the EMC simulation tool GeckoEMC [6] is explained in more detail in this section.

A. Theory of PEEC-BIM Coupled Method

In order to model the influence of magnetic materials with PEEC, the homogenization technique is used, i.e., a magnetic core is characterized as homogeneous linear material defined by the relative permeability coefficient $\mu_{\rm r}$. Therefore, the research relies on the corresponding permeability curves measured or provided by manufacturers, as is typically done in practice for the selection and design of inductors.

An investigation of different winding configurations has helped to understand better the EM influence of a magnetic core. The results point out that the winding arrangement, i.e., the specified distribution of the excitation currents, determines the nature of the fictitious magnetic currents. Practical toroidal coils with rectangular cross section and N turns are wound such that they can be represented as a superposition of a circular loop and N rectangular rings along the core circumference [10]. For this kind of excitation, the simulation results and measurements prove that $\vec{K}_{{\rm M}\varphi}$, the magnetic surface currents in the "main" direction, forming loops around the core [cf. Fig. 1] are sufficient to model the EM behavior of the core and winding. As a result, in comparison to the research presented in [11], it is shown that the magnetic surface current density $\vec{K}_{{\rm M}\theta}$ and/or surface charge density $\sigma_{\rm M}$ do not have a significant influence on the EM behavior of toroidal inductors with closed magnetic path, and the computational problem can be reduced to the calculation of only $\vec{K}_{{\rm M}\varphi}$ magnetic surface currents, i.e., $\vec{K}_{\rm M} \approx \vec{K}_{{\rm M}\varphi}$. The numerical implementation of the developed PEEC-BIM coupled method is based on the discretization of the core surface into $N_{\rm M}$ panels carrying the fictitious surface currents $\vec{K}_{{\rm M}k}$ $(k = 1 \ldots N_{\rm M})$ in the $\vec{i}_{\rm r}$- or $\vec{i}_{\rm n}$-directions as described in Fig. 1.

The magnetic surface current density $\vec{K}_{\rm M}$ is represented by rectangular pulse functions [15] so that the kth magnetic panel carries the total current $I_{{\rm M}k}$ distributed over the panel width $l_{{\rm M}k}$, and the approximated magnetic surface current $K_{{\rm M}k}$ at the kth magnetic panel is given by

$$K_{\rm Mk} = \frac{I_{\rm Mk}}{l_{\rm Mk}}. \tag{1}$$

The PEEC mesh of the winding consists of $N_{\rm J}$ cylindrical PEEC cells of the volumes ${\rm Vol}_j$, $j = 1 \ldots N_{\rm J}$. Rectangular pulse-basis functions are also used for the discretization of the winding current distribution and a filament approach is used to calculate $\vec{H}$ field contribution of the current $\vec{I}_j$ within the volume ${\rm Vol}_j$. Following the standard PEEC approach for electric field modeling, the charge density over the corresponding

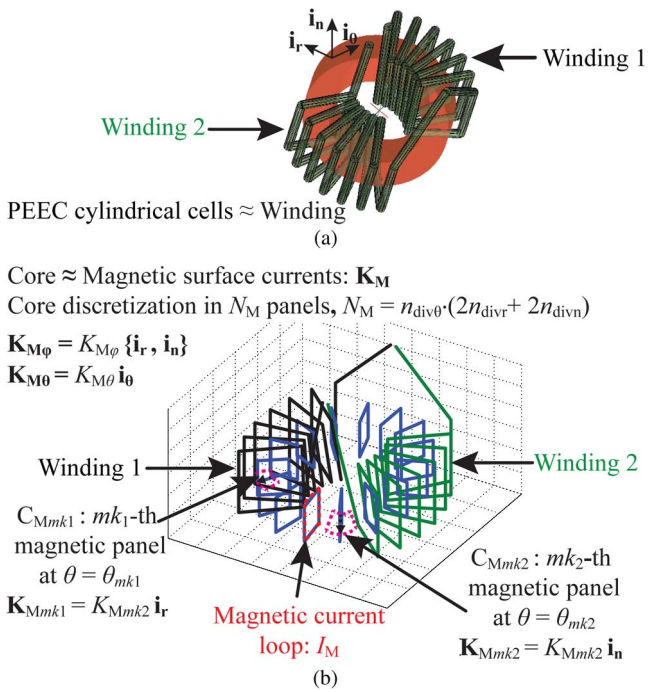

Fig. 1. PEEC-BIM modeling of a single-phase CM inductor with DM winding configuration: (a) GeckoEMC model and (b) the model description.

volume cells is discretized into N_N PEEC surface cells, employing the same type of mesh [15].

The correlation between the excitation (electric) currents and the fictitious magnetic surface currents is achieved via the boundary conditions for the tangential component of magnetic field strength $\vec{H}_\mathrm{t}$ that have to be satisfied at the surface of the magnetic core. Accordingly, the $\vec{H}_\mathrm{t}$ boundary condition at the center point of the kth magnetic panel $\mathrm{C}_{\mathrm{M}k}$ is given by (2), where $\vec{n}_{\mathrm{M}k}$ is the normal surface vector.

$$\left(\frac{\vec{B}_{\mathrm{coil(M}k)}}{\mu_0}+\frac{\vec{B}_{\mathrm{M(M}k)}}{\mu_0}\right)\times\vec{n}_{\mathrm{M}k}=\left(1+\frac{1}{\mu_\mathrm{r}-1}\right)\vec{K}_{\mathrm{M(M}k)} \tag{2}$$

where $\vec{B}_{\mathrm{coil(M}k)}=\vec{B}_{\mathrm{coil}}(\mathrm{C}_{\mathrm{M}k})$ is the magnetic field generated by the winding and $\vec{B}_{\mathrm{M(M}k)}=\vec{B}_{\mathrm{M}}(\mathrm{C}_{\mathrm{M}k})$ is the magnetic field from the magnetic surface current distribution $\vec{K}_\mathrm{M}$, both calculated at the position of $\mathrm{C}_{\mathrm{M}k}$. If the influence of the kth magnetic panel to itself, i.e., the singularity point, is distinguished within the total vector, i.e., $\vec{B}_{\mathrm{M/M}k\mathrm{(M}k)}$, then (2) can be rewritten in the form of

$$\left(\frac{\vec{B}_{\mathrm{coil(M}k)}}{\mu_0}+\frac{\vec{B}_{\mathrm{M/M}k\mathrm{(M}k)}}{\mu_0}\right)\times\vec{n}_{\mathrm{M}k}-\left(\frac{1}{2}+\frac{1}{\mu_\mathrm{r}-1}\right)\vec{K}_{\mathrm{M}k}=0 \tag{3}$$

and then further translated in the matrix form as in

$$\boldsymbol{\lambda}_\mathrm{MI}\mathbf{I}+\boldsymbol{\alpha}_\mathrm{MM}\mathbf{K}_\mathrm{M}=0. \tag{4}$$

The matrix entries of $\boldsymbol{\alpha}_\mathrm{MM}$ (5) and $\boldsymbol{\lambda}_\mathrm{MI}$ (6) are derived from the Biot–Savart law considering the winding and $\vec{K}_\mathrm{M}$ currents as sources of magnetic field

$$\alpha_\mathrm{MM}(mk,mj)=\left[\frac{1}{4\pi}\iint\limits_{S_{mj}}\frac{\vec{f}_\mathrm{M}(\vec{r}_{mj})\times(\vec{r}_{mk}-\vec{r}_{mj})}{|\vec{r}_{mk}-\vec{r}_{mj}|^3}\mathrm{d}S_{mj}\times\vec{n}_{mk}\right]\cdot\vec{f}_{\mathrm{M}mk} \tag{5}$$

$$\lambda_\mathrm{MI}(mk,j)=\left[\frac{1}{4\pi}\iiint\limits_{Vol_\mathrm{j}}\frac{\vec{f}(\vec{r}_j)\times(\vec{r}_{mk}-\vec{r}_j)}{|\vec{r}_{mk}-\vec{r}_j|^3}\mathrm{d}Vol_j\times\vec{n}_{mk}\right]\cdot\vec{f}_{\mathrm{M}mk} \tag{6}$$

where $\vec{r}_{mj}$ is the observation point lying on the mjth magnetic panel, S_{mj} is the area of the mjth magnetic panel, $\vec{f}_{\mathrm{M}mk}$ is the tangential unit vector defining the direction of the mkth magnetic surface current, i.e., $\vec{K}_{\mathrm{M}mk}=K_{\mathrm{M}mk\varphi}\cdot\vec{f}_{\mathrm{M}mk}$, $\vec{f}_{\mathrm{M}mk}$ is either $\vec{i}_r$ or $\vec{i}_n$ (Fig. 1). The singularity problem appears by the calculation of the diagonal matrix elements, $\alpha_\mathrm{MM}(mk,mk)=\alpha_{\mathrm{M}kk}$. The term $\alpha_{\mathrm{M}kk}=1/2$ in (3) originates from the Cauchy principal part of (2). The calculation of singular integrals is actually the main disadvantage of the BIM and also the main difficulty for the implementation of the PEEC-BIM method for arbitrary geometries. The calculation error arises because the mesh size has an obvious influence on the final results and the calculated singularity (the term $\alpha_{\mathrm{M}kk}=1/2$) does not depend on the panel size. Therefore, a modification of the $\alpha_{\mathrm{M}kk}$ coefficients was performed by enforcing the cancellation of the permeability free terms according to [16]. The calculation of the $\boldsymbol{\alpha}_\mathrm{MM}$ matrix turns to be the key point for a correct PEEC-based modeling of toroidal cores, which are typically used for EMI filter applications with μ_r in the range from approximately 10 up to $>10^5$.

Specifically, the extended PEEC system matrix, including the $\boldsymbol{\alpha}_\mathrm{MM}$ and $\boldsymbol{\lambda}_\mathrm{MI}$ matrix coefficients, is then defined by (7), where $\mathbf{A}(N_\mathrm{J}\times N_\mathrm{N})$ is the connectivity matrix defining the connection between PEEC partial elements, i.e., conductors, $\mathbf{R}$ is the resistance diagonal $(N_\mathrm{J}\times N_\mathrm{J})$ matrix, $\mathbf{L}$ is the inductance $(N_\mathrm{J}\times N_\mathrm{J})$ matrix consisting of the self- and mutual inductances between PEEC volume cells, $\mathbf{C}=\mathbf{P}^{-1}$ is the capacitance (potential) $(N_\mathrm{N}\times N_\mathrm{N})$ matrix defining the self- and mutual- potentials of PEEC surface cells, $\mathbf{Y}_\mathrm{L}$ is the admittance $(N_\mathrm{N}\times N_\mathrm{N})$ matrix consisting of matrix stamps of additional circuit elements connected between PEEC nodes, and $\mathbf{I}_\mathrm{S}$ and $\mathbf{V}_\mathrm{S}$ are current and voltage sources for modeled excitations. The $\mathbf{L}_\mathrm{M}$ $(N_\mathrm{J}\times N_\mathrm{M})$ matrix includes the mutual inductances between PEEC volume cells and the currents $\mathbf{K}_\mathrm{M}$. Optionally, magnetic and electric field strengths can be calculated in a postprocessing step via the distribution of the currents $\mathbf{I}$, potentials $\mathbf{V}$, and magnetic surface currents $\mathbf{K}_\mathrm{M}$.

$$\mathbf{M}_\mathrm{sys}=\begin{bmatrix}\mathbf{A} & -(\mathbf{R}+j\omega\mathbf{L}) & -j\omega\mathbf{L}_\mathrm{M}\\ (j\omega\mathbf{P}^{-1}+\mathbf{Y}_\mathrm{L}) & \mathbf{A}^\mathrm{T} & \mathbf{0}\\ \mathbf{0} & \boldsymbol{\lambda}_\mathrm{MI} & \boldsymbol{\alpha}_\mathrm{MM}\end{bmatrix}$$
$$\mathbf{M}_\mathrm{sys}\begin{bmatrix}\mathbf{V}\\ \mathbf{I}\\ \mathbf{K}_\mathrm{M}\end{bmatrix}=\begin{bmatrix}\mathbf{V}_\mathrm{S}\\ \mathbf{I}_\mathrm{S}\\ \mathbf{0}\end{bmatrix} \tag{7}$$

TABLE I
INDUCTOR SPECIFICATIONS 1

Type	Core manufacturer / core material / Core size / Initial μ	Winding (wire diameter)
S1a	Vacuumschmelz (VAC) / Vitoperm 500F / W380 core / $\mu \approx 10^5$ [17]	2 × 7 (1.4 mm)
S1b	custom made / Air (Plastic) / W380 core dimensions / $\mu \approx 1$	2 × 7 (1.4 mm)
S3	Micrometals / Iron powder / T94-26 core / $\mu^i \approx 75$ [18]	1 × 12 uniform (1.4 mm)

TABLE II
INDUCTOR SPECIFICATIONS 2

Type	Core manufacturer / Core material / Core size / Initial μ	Windings (wire diameter)
S2a	ArcelorMittal / K_ / KJ 030 020 Y 200 core / $\mu_i \approx 200$ [19]	2×7 turns (1.4 mm)
S2b	ArcelorMittal / K_ / KJ 030 020 Y 1000 core / $\mu_i \approx 1000$ [19]	2×7 turns (1.4 mm)
S2c	ArcelorMittal / Nanocristalline Nanophy /N47B3 core /$\mu_i > 200000$ [19]	2×7 turns (1.4 mm)
S2d	custom made / air (plastic) / KJ 030 020 Y 200 core dimensions /$\mu_i \approx 1$	2×7 turns (1.4 mm)

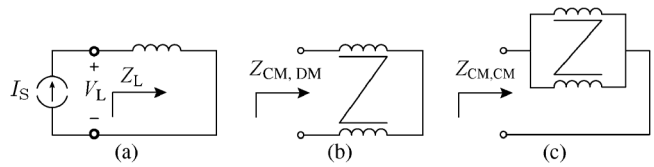

Fig. 2. Winding configuration for the measurements of (a) DM inductor impedance, (b) leakage impedance of CM inductor $Z_{\mathrm{CM,DM}}$, and (c) main impedance of CM inductor $Z_{\mathrm{CM,CM}}$.

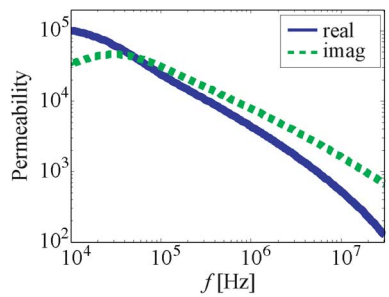

Fig. 3. Permeability curves, $\mu'(f)$ and $\mu''(f)$, used as the input parameters in the simulation of the $S1a$ inductor specified in Table I.

B. Simplified PEEC-BIM Coupled Method

The comparison between different winding arrangement and cores regarding the generated magnetic field inside and outside of the core in the experiments has been used to explain the EM behavior of the inductor and allowed further simplification of the PEEC-BIM model. The magnetic panels, belonging to the same magnetic current loop at the angle θ_k are merged together, so that they define one unknown $I_{\mathrm{M}k}$, $k = 1 \ldots n_{\mathrm{div}\theta}$. Namely, the $\boldsymbol{\alpha}_{\mathrm{MM}}(N_{\mathrm{M}} \times N_{\mathrm{M}})$, $\boldsymbol{\lambda}_{\mathrm{MI}}(N_{\mathrm{M}} \times N_{\mathrm{J}})$, and $\mathbf{L}_{\mathrm{M}}(N_{\mathrm{J}} \times N_{\mathrm{M}})$ matrices are first calculated. Then, through an averaging process, the matrices are reduced to $\boldsymbol{\alpha}_{\mathrm{MMavg}}(n_{\mathrm{div}\theta} \times n_{\mathrm{div}\theta})$, $\boldsymbol{\lambda}_{\mathrm{MIavg}}(n_{\mathrm{div}\theta} \times N_{\mathrm{J}})$, and $\mathbf{L}_{\mathrm{Mavg}}(N_{\mathrm{J}} \times n_{\mathrm{div}\theta})$ matrices, so that the PEEC-BIM system matrix takes the form of

$$\mathbf{M}_{\mathrm{sys}} = \begin{bmatrix} \mathbf{A} & -(\mathbf{R}+j\omega\mathbf{L}) & -j\omega\mathbf{L}_{\mathrm{Mavg}} \\ (j\omega\mathbf{P}^{-1}+\mathbf{Y}_{\mathrm{L}}) & \mathbf{A}^{\mathrm{T}} & \mathbf{0} \\ \mathbf{0} & \boldsymbol{\lambda}_{\mathrm{MIavg}} & \boldsymbol{\alpha}_{\mathrm{MMavg}} \end{bmatrix} \tag{8a}$$

$$\mathbf{M}_{\mathrm{sys}} \begin{bmatrix} \mathbf{V} \\ \mathbf{I} \\ \mathbf{I}_{\mathrm{M}} \end{bmatrix} = \begin{bmatrix} \mathbf{V}_{\mathrm{S}} \\ \mathbf{I}_{\mathrm{S}} \\ \mathbf{0} \end{bmatrix}. \tag{8b}$$

Therefore, the number of additional unknowns in the simplified PEEC-BIM model is reduced to $n_{\mathrm{div}\theta}$ loops carrying the magnetic currents $\mathbf{I}_{\mathrm{M}}$, which is significantly less than the number of magnetic panels N_{M}, $N_{\mathrm{M}} = n_{\mathrm{div}\theta} \cdot (2 \cdot n_{\mathrm{divr}} + 2 \cdot n_{\mathrm{divn}})$, carrying the magnetic surface currents $\mathbf{K}_{\mathrm{M}}$ (cf. Fig. 1). This simplified PEEC-BIM approach, finally implemented in the software GeckoEMC, was verified by both impedance and near-field measurements of different inductors. The verification results are presented in the next section.

IV. VERIFICATION OF THE PROPOSED PEEC-BIM METHOD

In this paper, two main aspects are investigated:

1) PEEC-based modeling of DM inductors (Z_{L}) and of single-phase CM inductors including the CM ($Z_{\mathrm{CM,CM}}$) and DM impedances ($Z_{\mathrm{CM,DM}}$) and
2) PEEC-based modeling of the mutual coupling between an inductor and a pick-up coil.

The specifications of the investigated inductors used in the PEEC-BIM simulation are given in Tables I and II. The frequency range of interest is within 150 kHz to 30 MHz, as defined by the EMC standards for conducted emissions.

A. PEEC-BIM Simulation Versus Measurements of Impedance

The PEEC-BIM simulation of inductor impedances was verified for DM and CM winding configurations (cf. Fig. 2), of single-phase CM inductors ($S1a$, cf. Table I; $S2a$–d, cf. Table II), and for a DM inductor with a uniform one-layer winding arrangement ($S3$, cf. Table I).

The impedance of an inductor, Z_{L}, is calculated from the PEEC-BIM circuit shown in Fig. 2(a) as

$$Z_{\mathrm{L}} = \frac{V_{\mathrm{L}}}{I_{\mathrm{S}}} \tag{9}$$

where $I_{\mathrm{S}} = 1$ A is the current source set at the terminals of the inductor, and V_{L} is the voltage across the terminals calculated from (8). A comparison between the simulation and the corresponding measurement results is shown for the inductors defined in Tables I and II, respectively, in Figs. 4 and 5. The simulation input parameters are the geometry and material properties of the winding and the core. The core permeability curves, i.e., $\underline{\mu}(f) = \mu'(f) - j\mu''(f)$, used in the simulation, were extracted from the impedance measurements of the inductors with uniform winding arrangement and low number of turns (typically 1 × 5 turns uniform winding). The permeability curves used as the input parameters in the simulation of the $S1a$ inductor, which is specified in Table I, are shown in Fig. 3 as an example. The $\mu'(f)$ and $\mu''(f)$ curves are extracted from the impedance measurements of an inductor with three turns built on a VAC W380 core.

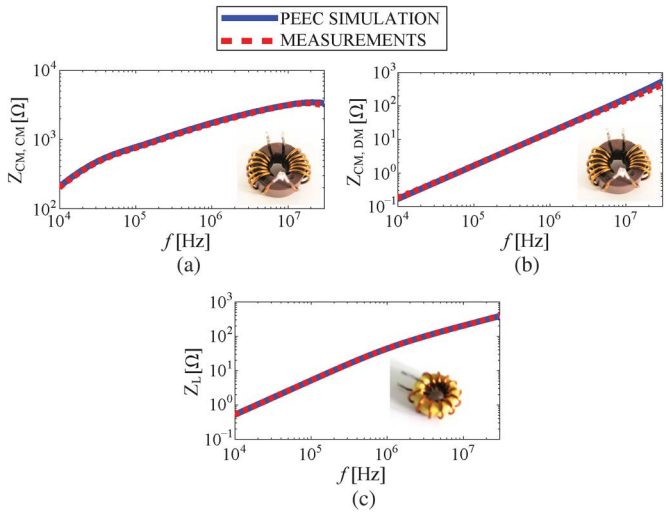

Fig. 4. Comparison between PEEC-BIM simulation and measurements of: (a) CM impedance $Z_{\mathrm{CM,CM}}$ and (b) DM impedance $Z_{\mathrm{CM,DM}}$, of the single-phase $S1a$ inductor, and (c) the total impedance Z_{L} of the $S3$ inductor (cf. Table I).

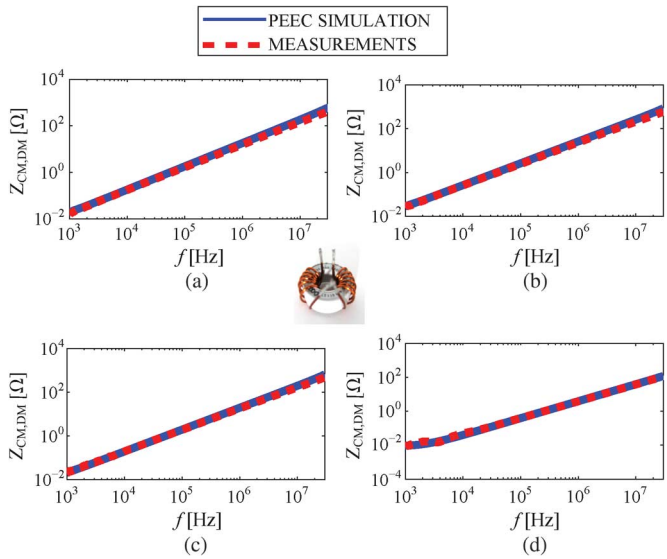

Fig. 5. Comparison between PEEC-BIM simulation and measurements of DM impedance $Z_{\mathrm{CM,DM}}$ of the single-phase: (a) $S2a$, (b) $S2b$, (c) $S2c$, and (d) $S2d$ inductors (cf. Table II).

For better results at higher frequencies above 20 MHz, more accurate measurements of the permeability $\mu_{\mathrm{r}}(f)$ would be required. The other high-frequency effects that determine the inductor impedance are the effect of the parasitic capacitances, i.e. turn-to-turn and turn-to-core capacitances, and the skin and proximity effects. The skin and proximity effects are taken into account by the ac wire resistance, R_{ac} [as the elements of the $\mathbf{R}$-matrix in (8a)], and the higher discretization of the PEEC cells, respectively. It was shown in [20] that the PEEC-BIM modeling can be used to accurately model the capacitive effects in toroidal magnetic inductors, and hence, the PEEC-BIM modeling of the stray field generated by toroidal inductors is addressed in this paper in more detail.

A single-phase CM choke (i.e. an inductor with a nonuniform winding arrangement) is examined in order to understand and model the EM influence of the magnetic core material. A CM choke can be characterized by the high CM inductance $L_{\mathrm{CM,CM}}$ achieved with high permeability CM cores ($\mu_{\mathrm{r}} = \mu_{\mathrm{CM}}$) and its DM leakage inductance $L_{\mathrm{CM,DM}}$, which can be used to suppress high-frequency DM currents. However, the leakage inductance has to be controlled to prevent core saturation at high line currents, implying that an optimal design of a CM choke has to be found. According to [21], the leakage flux is mainly determined by the flux path through air, which is, in turn, defined by the winding and core geometry rather than the permeability of the core. As a result, the factor of an effective permeability ($\mu_{\mathrm{CM,DM}} = \mu_{\mathrm{eff}}$) was introduced in [21] to model the leakage inductance $L_{\mathrm{CM,DM}}$ of a single-phase CM toroidal inductor. The μ_{eff} factor quantitatively describes the influence of the core on the leakage flux, i.e. the increase of $L_{\mathrm{CM,DM}}$ due to the presence of the core

$$\begin{aligned} Z_{\mathrm{CM,DMcore}} &= \mu_{\mathrm{eff}} Z_{\mathrm{CM,DMair}} \\ \Rightarrow L_{\mathrm{CM,DMcore}} &= \mu_{\mathrm{eff}} L_{\mathrm{CM,DMair}}. \end{aligned} \tag{10}$$

As in [21], $L_{\mathrm{CM,DMair}}$ is determined by the winding geometry, i.e., the angle coverage of the winding, while μ_{eff} is defined only by the core geometry (the cross section A_{e} and the effective path length l_{e} of the toroid) and not by its magnetic properties:

$$\mu_{\mathrm{eff}} = 2.5\Gamma^{1.45}, \quad \Gamma = \sqrt{\frac{\pi}{A_{\mathrm{e}}}}\frac{l_{\mathrm{e}}}{2}. \tag{11}$$

Following this model of leakage inductance, the authors in [9] developed the PEEC equivalent circuit of a CM inductor, assuming that the magnetic core material does not change the magnetic field lines outside the core. Thus, all mutual inductive couplings M from the inductor were calculated in air and then multiplied by the factor of μ_{eff}. Therefore, in this paper, four samples $S2a$–d having cores of same dimensions (outer diameter $OD = 30$ mm, inner diameter $ID = 20$ mm, and core height $h = 10$ mm) but with different initial permeability values of $\mu_{\mathrm{eff}} = \{1, 200, 1000, > 10^5\}$ were used to obtain a better insight into the physical meaning of μ_{eff}.

The measurement results in Fig. 5 imply a $\mu_{\mathrm{eff}} = 4.5$ for the observed winding/core geometry as the measured DM inductances of $S2a$, $S2b$, and $S2c$ inductors are $L_{\mathrm{CM,DM}} \approx 2.8\ \mu$H and the DM inductance of the air inductor $S2d$ is $L_{\mathrm{CM,DM}} \approx 0.63\ \mu$H. The results also show that μ_{eff} weakly depends on μ_{CM} for high permeability cores typically used for CM inductors. However, the influence of the core on the magnetic stray field cannot be understood from the impedance plots shown in Fig. 5 and, hence, near-field measurements, i.e., magnetic coupling measurements, were performed to show whether μ_{eff} can be used as a modification factor that would allow for neglecting the presence of the core material, as its was assumed in [9] and [10].

B. EM Coupling Measurement Setup

The test setup for the field measurements consists of a power amplifier impressing a sinusoidal voltage at the terminals of the inductor and a pick-up coil to verify the magnetic flux density

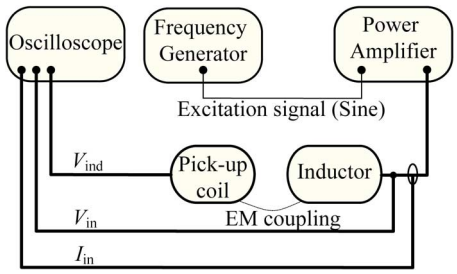

Fig. 6. Measurement setup schematic.

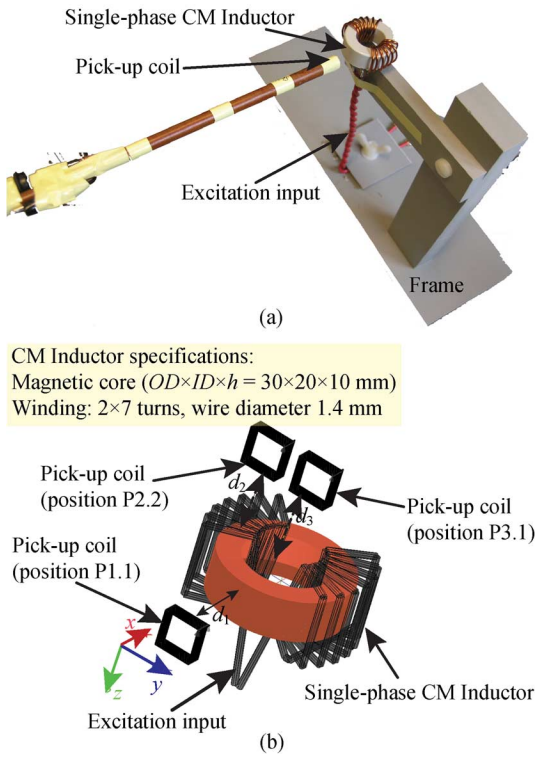

Fig. 7. Electromagnetic coupling effect between a single-phase CM inductor with DM winding configuration and a pick-up coil: (a) measurement setup and (b) GeckoEMC model.

by measuring the induced voltage using a high precision oscilloscope (cf. Fig. 6).

The used single-layer pick-up coil is built of 15 turns (copper wire diameter 0.2 mm) on a cylindrical coil former (diameter 8 mm). To investigate the influence of the magnetic core on the stray field, the injected current $I_{\rm in}$, the input voltage $V_{\rm in}$, and the induced sensor voltage $V_{\rm ind}$ are measured. Three positions of the pick-up coil, P1.1, P2.2, and P3.1, were selected, as shown in Fig. 7, in order to track the dominant component of the $\vec{H}$-field (cf. Fig. 8). In Figs. 7(b) and 8, the sensor has a rectangular shape with the same cross section area as the used 15 turns pick-up coil. A comparison between the PEEC-BIM simulation and the measurements of the mutual coupling for $S1a$–b at $f = 10$ kHz is presented in Fig. 9, showing good agreement between the simulated and measured values with a difference less than 2 dB. This confirms the applicability of the measurement setup for further investigations performed to evaluate the influence of the magnetic core on the stray field of inductors.

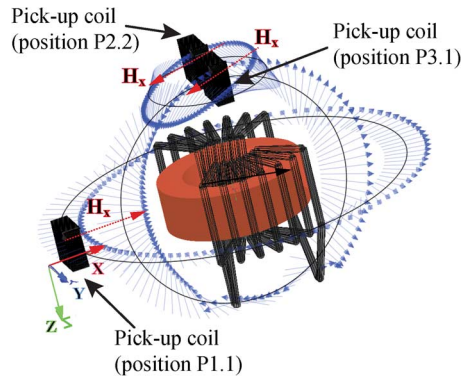

Fig. 8. GeckoEMC simulation of magnetic field vectors from a single-phase CM inductor with DM winding configuration, showing the dominant $\vec{H}$-field components.

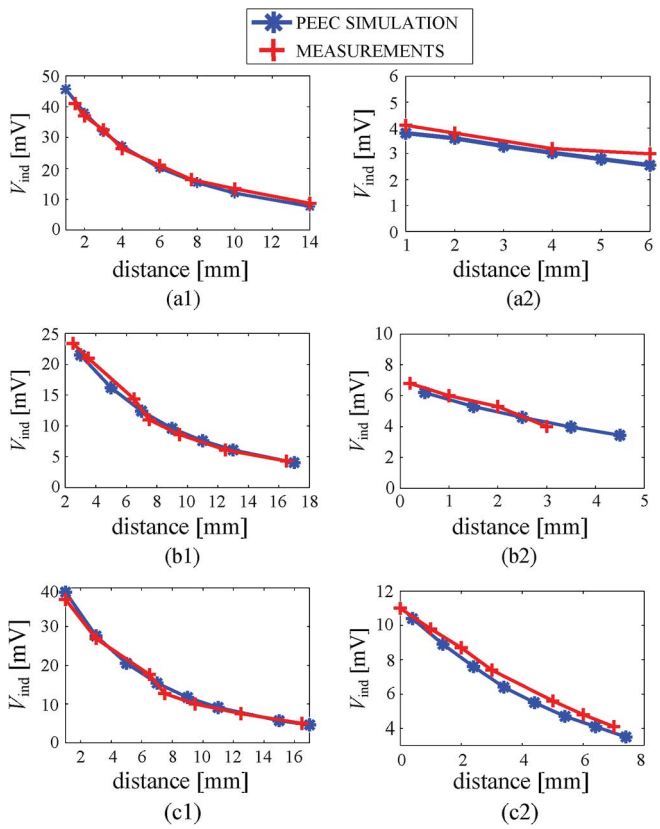

Fig. 9. Comparison between PEEC simulation and measurements of the induced voltage in the pick-up coil for three pick-up coil positions at $f = 10$ kHz, $I_{\rm in} = 3$ A: (a1) $S1a$ at P1.1, (a2) $S1b$ at P1.1, (b1) $S1a$ at P2.2, (b2) $S1b$ at P2.2, (c1) $S1a$ at P3.1, and (c2) $S1b$ at P3.1.

C. PEEC-BIM Simulation Versus Measurements of EM Coupling

The influence of the magnetic core on the stray field of inductors was investigated by observing the inductors with cores of same sizes but different $\mu_{\rm r}$ value (cf. Table II $S2$ core type). The PEEC-BIM approach was verified with both the measurement results and corresponding magneto-static FEM simulations. The DM winding configuration of a single-phase CM inductor, i.e., $Z_{\rm CM,DM}$ Fig. 1, is used for the modeling and calculation of magnetic coupling effects and to assess the modeling approach of

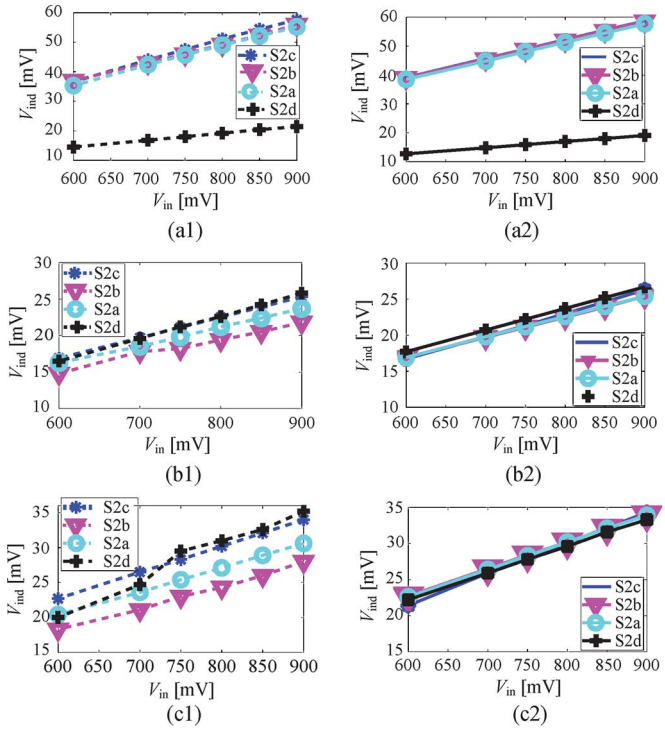

Fig. 10. The induced voltage in the pick-up coil for three coil positions (a) P1.1, (b) P2.2, (c) P3.1, at $f = 80$ kHz, $V_{in} = \{600\text{ mV}, 700\text{ mV}, 800\text{ mV}, 850\text{ mV}, 900\text{ mV}\}$: 1) measurements and 2) PEEC-BIM simulations.

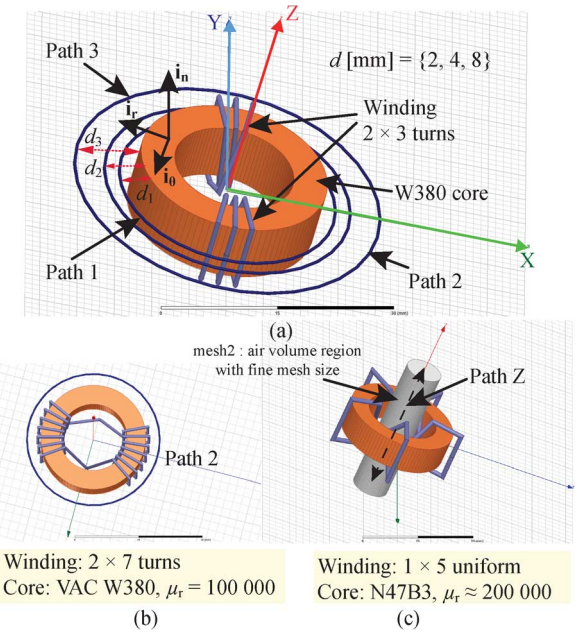

Fig. 11. Examples used for the comparison of the PEEC-BIM and FEM-based simulations of (a) a single-phase CM inductor with low number of turns (2 × 3 turns), (b) a single-phase CM inductor with higher number of turns (2 × 7 turns), and (c) a uniform 1 × 5 turns winding.

the leakage inductance of the single-phase CM inductor, as described in the previous subsection. A sinusoidal voltage signal with constant amplitude $V_{in} = V_{IN}$ was applied at the terminals of the air-core $(S2d)$ and magnetic core inductors ($S2a$, $S2b$, and $S2c$) so that the relation between the input current I_{in} and V_{IN} is given by

$$V_{in,air} = V_{IN} = Z_{CM,DMair} I_{in,air}$$
$$V_{in,core} = V_{IN} = Z_{CM,DMair} \mu_{eff} I_{in,core}. \quad (12)$$

Assuming that the magnetic field lines are not influenced by the core material as it is proposed in [9], a μ_{eff} times higher input current is required for $S2d$ than for $S2a$–c in order to obtain the same induced voltage $V_{ind} = V_{IND}$ in the pick-up coil for all pick-up coil (sensor) positions that is described by

$$V_{ind,air} = V_{IND} = M_{air} I_{in,air},$$
$$V_{ind,core} = V_{IND} = M_{core} I_{in,core} = M_{air} \mu_{eff} I_{in,core}. \quad (13)$$

However, the analysis performed in this paper did not show such behavior. The measurement and PEEC simulation results of V_{ind} are presented in Fig. 10 for three different pick-up coil positions, and the input voltages of $V_{in} = \{600\text{ mV}, 700\text{ mV}, 800\text{ mV}, 850\text{ mV}, 900\text{ mV}\}$ and the required input currents. The difference of approximately 5 dB between the PEEC-BIM simulation and the measurement results of V_{ind} originates from the accuracy limit of the measurement setup.

The results in Fig. 10(a) show that the mutual coupling cannot be described by μ_{eff} for all directions in space around the toroidal inductor. Fig. 10(a1) and 10(a2) illustrate that V_{ind} is increased due to the presence of the magnetic core for the position P1.1. Namely, the core cannot be included into a PEEC simulation just by the factor of effective permeability μ_{eff}, but the field lines are influenced by the magnetic core. This change of magnetic field lines due to the core is discussed in more detail in the next subsection.

D. Stray Field Lines of Toroidal Inductors

The low-frequency PEEC-BIM and a corresponding Maxwell3D v15.0) finite-element simulation of the near magnetostatic field lines were performed for different directions and distances from the inductor. The $\vec{H}$ field components are calculated at the points of a circular curve around single-phase CM inductors at the distance of 2, 4, and 8 mm from the core and at Z-axis (cf. Fig. 11) Path 1–3, and Path Z.

The comparison of the calculated $\vec{H}$ field components in the FEM-based simulator Maxwell3D, and the PEEC-BIM simulation environment GeckoEMC is given in Figs. 12 and 13.

The highest mismatch between the simulation results and the measurements is approximately 5%. It is demonstrated that in the case of a low number of turns [cf. Fig. 11(c)], the stray field lines are modified due to the presence of the core especially near the core sections which are not covered by the windings (cf. Fig. 14). The influence of the magnetic core on the direction of the magnetic field lines decreases if the core is fully covered with windings and additionally diminishes with increasing distance. Namely, the direction of the magnetic field lines is changed due to the presence of magnetic core in the case of the inductors with nonuniform winding arrangements, and it is much less influenced by the core for the inductors with uniform windings.

The developed PEEC-BIM simulation provides an explanation of the EM behavior of inductors: the major core

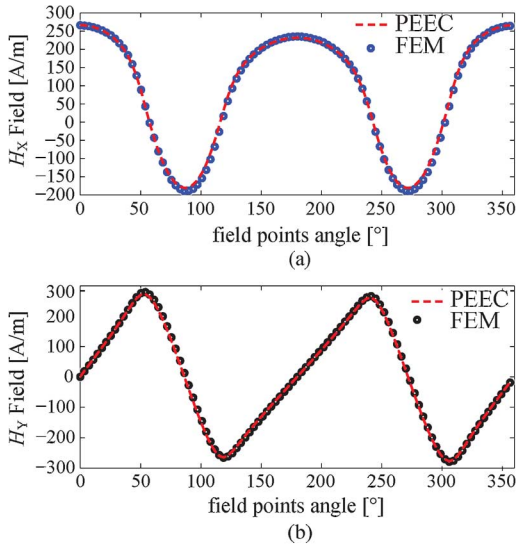

Fig. 12. GeckoEMC PEEC-BIM versus Maxwell3D FEM magnetostatic simulations of dominant (a) H_X- and (b) H_Y-magnetic field components at the points of a circular curve (4 mm from the core) around a single-phase CM inductor (2×7 turns, VAC VITROPERM 500F W380 core) with DM winding configuration [cf. Fig. 11(b)]; the z-component is not shown since $H_Z \ll H_X, H_Y$.

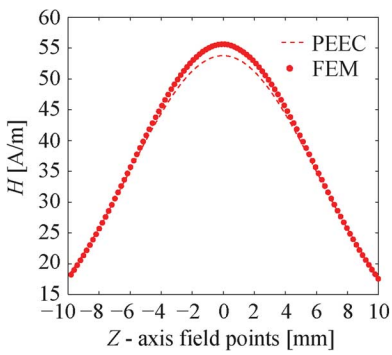

Fig. 13. GeckoEMC PEEC-BIM versus Maxwell3D FEM magneto-static simulations of dominant magnetic field component H_Z at points of the z-axis from a uniform $1\times$ 5 turns winding on N47B3 core [cf. Fig. 11(c)]; the x and y components are not shown since $H_Z \gg H_X, H_Y$.

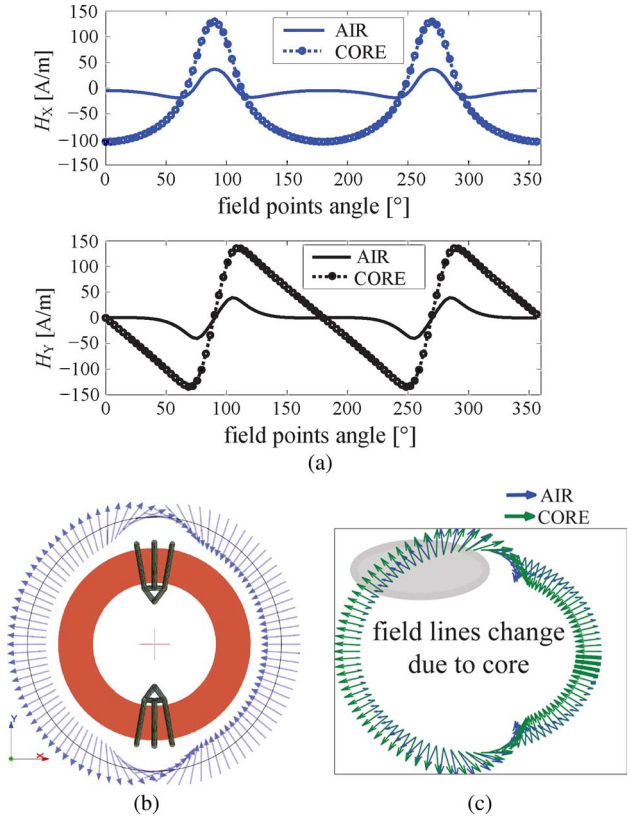

Fig. 14. GeckoEMC simulation of single-phase 2×3 turns CM inductors shown in Fig. 11(a) with VAC VITROPERM 500F W380 core and AIR W380 core: (a) dominant H-field components, (b) H-field vectors, and (c) change of field vectors due to the magnetic core at the points of a circular curve with the distance of 4 mm from the core surface.

contribution to the magnetic leakage field can be ascribed to the magnetic surface currents forming loops around the core. The strength of these currents is higher on the parts of the core covered by windings, and they are proportional to the core permeability. Consequently, the analysis implies that neither neglecting the presence of the core [10] nor the usage of the factor μ_{eff} [9] is a comprehensive approach. Furthermore, the results show that the proposed PEEC-BIM approach facilitates direct modeling of the EM behavior of toroidal inductors without using the effective permeability μ_{eff}.

V. PEEC-BIM Simulation Performance

Every electromagnetic simulation has to be initialized by the input parameters that can be classified as geometrical (e.g., winding and core geometry), material (e.g., core properties), and numerical (e.g., mesh). The accuracy of simulation depends on the simulation settings, which should correspond to the actual system as close as it is possible. It was observed that the winding geometry does not represent a critical input parameter and that the mesh of the magnetic surface in $\vec{i}_{\text{r}}$, $\vec{i}_{\theta}$, and $\vec{i}_{\text{n}}$ directions determines the computational complexity and accuracy of the implemented PEEC-BIM method (cf. Fig. 1). Contrary to the PEEC-BIM method, in FEM simulations, a finite vacuum-region around the model has to be defined and the finite-element modeling of volumes with significant differences of magnetic properties requires a mesh refinement, which all increase computational time. In the PEEC simulation, a finer mesh means higher number of magnetic current loops, i.e., increasing $n_{\text{div}\theta}$, while for the FEM simulation, a finer mesh is the smaller mesh length size within the selected volume region [e.g., Fig. 11(c)]. The accuracy of the magnetic field vector simulation is more sensitive to the mesh size than the accuracy of the calculated inductance. The performance of the PEEC and FEM simulations are summarized in Table III, showing two mesh patterns, mesh 1 and mesh 2, with more and less precision, respectively. The simulations were performed on PCs with an Intel(R) Xeon(R) processor with two cores, 48 GB RAM and CPU clock frequency of 2.4 GHz. The choice of the PEEC method for modeling of conductors is clearly justifiable by the last two examples in Table III. The other examples are used to show the performance of the implemented PEEC-BIM approach. According to the simulation time results given in Table III, the PEEC-BIM simulation is at least twice faster than the corresponding FEM analysis, for a single magnetic

TABLE III
GECKOEMC PEEC-BIM VERSUS MAXWELL3D FEM SIMULATION RESULTS

Simulation	Simulation Settings mesh 1(mesh 2)	Results & Performance mesh 1 (mesh2)
PEEC: Fig. 11(c)	core mesh: $20(60) \times 5 \times 5$	L = 3.74 mH, tsim = 30 s (3 min)
FEM: Fig. 11(c)	mesh 1 (mesh 2)	L = 3.799 mH, tsim = 4 min (11 min)
PEEC: Fig. 11(b)	core mesh: $35(120) \times 5 \times 5$	L = 3.29 μH, tsim = 1 min (13 min)
FEM: Fig. 11(b)	mesh 1 (mesh 2)	L = 3.49 μH, tsim = 25 min (35 min)
PEEC: Fig. 11(b) air core μ = 1	/	L = 454.2 nH, tsim = 10 s
FEM: Fig. 11(b) air core μ = 1	mesh 1 (mesh 2)	L = 452.7 nH, tsim = 18 min (37 min)

component. Moreover, the developed PEEC-BIM model of inductors enables comprehensive analysis of inductors and, hence, allows fast and accurate modeling of inductors both as a separate component and as a part of a system [22]. This comparison between the PEEC-BIM and FEM-based simulations shows the advantages of the PEEC method for modeling the 3D geometries typically used in power electronics.

VI. CONCLUSION

The proposed PEEC-BIM-based model of toroidal inductors, including the simplification with magnetic current loops enables accurate modeling of more complex circuits, e.g., single/two-stage EMI filter structures [22]. The PEEC-BIM approach demonstrates less computational effort than is required for a corresponding FEM-based analysis. In addition, it offers a possibility of virtual prototyping in an efficient way employing the PEEC-BIM-based 3D simulation environment.

ACKNOWLEDGMENT

The authors would like to thank ArcelorMittal Amilly for supporting this research by providing core samples.

REFERENCES

[1] S. Wang, F. C. Lee, D. Y. Chen, and W. G. Odendaal, "Effects of parasitic parameters on EMI filter performance," *IEEE Trans. Power Electron.*, vol. 19, no. 3, pp. 869–877, 2004.

[2] A. Muesing, J. Ekman, and J. W. Kolar, "Efficient calculation of non-orthogonal partial elements for the PEEC method," *IEEE Trans. Magn.*, vol. 45, no. 3, pp. 1140–1143, Mar. 2009.

[3] G. Antonini, A. E. Ruehli, and C. Yang, "PEEC modeling of dispersive and lossy dielectrics," *IEEE Trans. Adv. Packag.*, vol. 31, no. 4, pp. 768–782, 2008.

[4] A. E. Ruehli, G. Antonini, and A. Orlandi, "Extension of the partial element equivalent circuit method to non-rectangular geometries," in *Proc. IEEE Int Electromagn. Compat. Symp.*, 1999, vol. 2, pp. 728–733.

[5] W. Yahyaoui, L. Pichon, and F. Duval, "A 3D PEEC method for the prediction of radiated fields from automotive cables," *IEEE Trans. Magn.*, vol. 46, no. 8, pp. 3053–3056, Aug. 2010.

[6] GeckoResearch, GeckoCIRCUIT/GeckoEMC [Online]. Available: http://www.gecko-research.com

[7] T.-S. Tran, G. Meunier, P. Labie, and J. Aime, "Comparison of FEM-PEEC coupled method and finite-element method," *IEEE Trans. Magn.*, vol. 46, no. 4, pp. 996–999, Apr. 2010.

[8] V. Ardon, J. Aime, O. Chadebec, E. Clavel, J.-M. Guichon, and E. Vialardi, "EMC modeling of an industrial variable speed drive with an adapted PEEC method," *IEEE Trans. Magn.*, vol. 46, no. 8, pp. 2892–2898, Aug. 2010.

[9] E. Hoene, A. Lissner, S. Weber, S. Guttowski, W. John, and H. Reichl, "Simulating electromagnetic interactions in high power density inverters," in *Proc. IEEE 36th Power Electron. Specialists Conf. (PESC)*, 2005, pp. 1665–1670.

[10] T. De Oliveira, J. Schanen, J. Guichon, and L. Gerbaud, "Automatic layout optimization of an EMC filter," in *Proc. IEEE Energy Convers. Congr. Expo. (ECCE)*, 2010, pp. 2679–2685.

[11] I. F. Kovacevic, A. Muesing, and J. W. Kolar, "An extension of PEEC method for magnetic materials modeling in frequency domain," *IEEE Trans. Magn.*, vol. 47, no. 5, pp. 910–913, May 2011.

[12] D. M. Cook, *The Theory of the Electromagnetic Field*. Englewood Cliffs, NJ, USA: Prentice-Hall, 1975.

[13] H. Long, Z. Feng, H. Feng, A. Wang, and T. Ren, "MagPEEC: Extended PEEC modeling for 3D arbitrary electro-magnetic devices with application for M-cored inductors," in *Proc. IEEE Radio Frequency Integr. Circuits (RFIC) Symp.*, 2003, pp. 251–254.

[14] G. Antonini, M. Sabatini, and G. Miscione, "PEEC modeling of linear magnetic materials," in *Proc. IEEE Int. Symp. Electromagn. Compat. (EMC)*, 2006, vol. 1, pp. 93–98.

[15] J. Ekman, "Electromagnetic modeling using the partial element equivalent circuit method" Ph.D. dissertation, Luleå Univ. of Technol., Luleå, Sweden, 2003 [Online]. Available: http://staff.www.ltu.se/jekman/Pres/PhDThesis.pdf

[16] T. Morisue, "3-D magnetostatic field calculation for a magnetic circuit with no (a narrow) air gap," *IEEE Trans. Magn.*, vol. 25, no. 5, pp. 3266–3268, Sep. 1989.

[17] Vacuumscmelze GmbH&Co, Nanocrystalline VITROPERM—EMC Products [Online]. Available: http://www.vacuumschmelze.com/

[18] Micrometals [Online]. Available: http://www.micrometals.com

[19] ArcelorMittal [Online]. Available: http://www.arcelormittal.com

[20] I. Kovacevic, T. Friedli, A. Muesing, and J. Kolar, "3D electromagnetic modeling of parasitics and mutual coupling in EMI filters," *IEEE Trans. Power Electron.*, to be published.

[21] M. Nave, *Power Line Filter Design for Switched-Mode Power Supplies*. New York, NY, USA: Springer, 1991.

[22] I. F. Kovacevic, T. Friedli, A. Muesing, and J. W. Kolar, "PEEC-based virtual design of EMI input filters," *Proc. IEEE Energy Convers. Congr. Expo. (ECCE)*, pp. 1935–1941, 2011.